Supersonic Flow Control of Swept Shock Wave/Boundary Layer Interaction using Plasma Actuators

Akshay S. Deshpande* and Jonathan Poggie†
Purdue University, West Lafayette, IN-47906

The effect of plasma actuators on the physics of the swept shock boundary layer interaction induced by a sharp fin is investigated in this paper by means of Reynolds-averaged Navier-Stokes calculations, using the SU2 code developed at Stanford University. The present work focuses on a sharp fin configuration placed in a Mach 5 flow, with a spatially developing turbulent boundary layer, at an angle of attack 12 deg. At the streamwise location of the fin leading edge, the Reynolds number based on momentum thickness and boundary layer thickness for the undisturbed boundary layer case are around 5075 and 3.321 mm, respectively. The mean pressure distribution and heat transfer data at the wall for the case without any actuators were compared to experimental data. The plasma actuator is modeled semi-empirically as a heating source and magnetic bodyforce term, which is included in the energy and momentum equations respectively. The plasma actuator is placed within the boundary layer at the upstream influence line to disturb the flow. A pair of horse-shoe vortices is created as the streamlines encounter the disturbance, which decay some distance downstream. The resulting time-averaged flow fields showed decreased intensity of the reflected shock wave, reduction in peak skin friction coefficient, and increase in the separation bubble length with plasma actuator control.

Nomenclature

B	Magnetic field	q	Imposed source term	ρ	Density
C_f	Skin friction coefficient	r	Radial distance measured from	θ	Momentum thickness
E	Total internal energy		the virtual conical origin	$\overline{\overline{\tau}}$	Shear stress tensor
F	Magnetic bodyforce	$\vec{v}$	Velocity vector	ω	Vorticity
I	Current	w	Characteristic length scale		
L	Length of the fin		of the source term	*Subscripts*	
Q	Power input	x	Streamwise direction	$\circ$	Reference values
R	Universal gas constant	y	Wall-normal direction	w	Wall quantities
Re	Reynolds number; $\rho_\infty U_\infty l/\mu$	z	Spanwise direction	∞	Free-stream quantities
S	Sutherland's constant	α	Angle of attack		
St	Stanton number	β	Azimuthal angle	*Superscripts*	
T	Static temperature	γ	Ratio of specific heats	$+$	Inner units
V	Voltage	δ	Boundary layer thickness	$\sim$	Non-dimensional quantities
c_p	Specific heat at constant pressure	δ^*	Displacement thickness	$'$	Distance downstream
c_v	Specific heat at constant volume	μ	Dynamic viscosity		of the actuator
p	Static pressure	ϕ	Inviscid shock wave angle		

*Graduate Research Assistant, School of Aeronautics and Astronautics, AIAA Student Member
†Associate Professor, School of Aeronautics and Astronautics, Associate Fellow AIAA

I. Introduction

Shock wave/boundary layer interaction (SWBLI) has been a topic of exhaustive research for the past several decades owing to its immutable complexity.[1,2] SWBLI occurs when a shock wave impinges on a viscous boundary layer, which leads to either an increase in its shape factor or separation from the surface. In almost all the cases, SWBLI has an adverse impact on the vehicle performance. Some of the effects include increased flow distortion in an engine inlet, enhanced drag on the wings, and aggravated thermal loads due to complex shock-shock interactions. In addition, SWBLI can cause unsteadiness which involves shock oscillations with frequencies an order of magnitude lower than than those associated with fine scale turbulence in the incoming boundary layer.[1,3] This can lead to fatigue loading which compromises the mechanical integrity of the structure.

Various flow control mechanisms have been devised to tackle these issues. The conventional approach has been achieved through mass transfer.[1] Methods such as boundary layer bleed/blowing aim to enhance the momentum of boundary layer, thereby making it more resistant to adverse pressure gradients. Boundary layer suction entails removal of low momentum portion near the wall to increase its shape factor and create a fuller profile. These techniques possess shortcomings such as increased weight due to additional plumbing, reduction in mass flow, and increased drag, which makes them inimical to internal flows.

Passive control of SWBLI by micro-vortex generators is an attractive alternative which compensates for the drawbacks mentioned above. This approach usually involves manipulation of flow-field by miniature geometric structures placed within the boundary layer to disturb the viscous flow. The mass transfer mentioned above is achieved by the counter-rotating vortices generated in the wake of the structure. In high-speed flows, these geometrical structures can be used to spread a strong shock system into a family of compression waves. This process effectively reduces the wave drag and efficiency loss associated with it by cutting down the entropy production.[4] Extensive studies by Babinsky et al.[4–7] on the performance of micro ramps have been carried out. Micro ramps have been found to reduce the separation extent/delay separation onset, but they are optimal for conditions in which the flow separation location is fixed and the generators can be placed relatively close upstream of the baseline separation.[8]

Plasma actuators overcome these impediments by offering advantages such as absence of any moving parts, minimal aerothermal penalty when not in operation, and quick response times to match the characteristic flow time scales.[9] Generally plasma actuators consist of two electrodes flush mounted on a dielectric surface. On applying a potential difference across the electrodes, a current is generated which forms an electrical discharge between the electrodes. If an external magnetic field is applied, a magnetic bodyforce is generated which can be aligned with the flow direction to increase the momentum of the boundary layer. They have recently gained huge attention for their variety of aerospace applications such as high speed drag reduction,[10,11] magneto-hydrodynamic (MHD) flow control,[9,12–19] flow-field manipulation using energy deposition,[10,11,20,21] controlling shock unsteadiness,[22–24] and flow bypass for Scramjet engines.[20] The effect of plasma actuators has been tested extensively both numerically and experimentally on compression ramps, which is essentially a two-dimensional interaction. The aim of this study is to test their versatility by applying them in a three-dimensional flow-field.

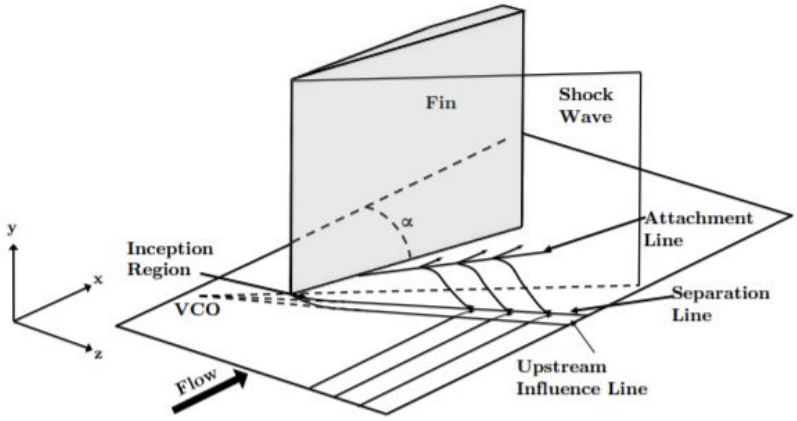

Figure 1. Three-dimensional sharp-fin interaction (Arora et al.[25])

The swept shock wave/boundary layer interactions investigated in this study are three-dimensional in nature, unlike unswept compression ramp flows which show minimal spanwise variation in mean quantities. Swept interactions can be further classified into dimensional interactions, which are characterized by an additional length scale of the shock wave generator, and dimensionless interactions, in which the flow is insensitive to any changes in the shock wave geometry.[4] Specifically, a sharp-fin is used as a shock generator for this study, and the flow can be characterized as a dimensionless interaction. Experiments carried out by Alvi and Settles[26] and Arora et al.[25,27] present a detailed description of the three-dimensional flow-field shown in Fig. 1. On examining the limiting streamlines, surface flow features such as the separation line, reattachment line, upstream influence line, and inviscid shock trace intersect at a point defined as the virtual conical origin (VCO), which lies upstream of the fin apex.[25] A unique feature of swept SWBLI's is their conical symmetry about the VCO; except in a region near the vicinity of the fin leading edge. This region is termed as the inception region.

This three-dimensional flowfield was studied numerically using Reynolds-averaged Navier-Stokes calculations by SU2, an open source multi-physics code developed at Stanford University. Once the results were validated with experimental data, a semi-empirical model of a plasma actuator was implemented by adding source terms to the momentum and energy equations. The plasma actuator was placed at an arbitrary location along the upstream influence line, and its effect on the interaction was investigated. The performance of the actuator is judged by comparing the mean wall pressures and skin friction coefficient with the baseline case in a conical frame of reference.

II. Methods

This section describes the physical model, details of the numerical method, and implementation of the plasma actuator model. The simulation procedure was similar to the approach taken by Leger et al.[28] in computing the baseline Mach 5 flow over a sharp fin.

II.A. Flow configuration

The configurations and flow conditions were based on the experiments carried out by E. Schülein[29] at DLR, Germany. An unswept sharp-fin was mounted on a flat plate and inclined at an angle of attack $\alpha = 12°$. The freestream properties are given in Table 1 below.

Parameter	Value
u_∞	829 m/s
M	5.0
Re/m	37×10^6
T_∞	68.3 K
T_w	300 K
ρ_∞	0.204 kg/m^3
Δy^+	0.1

Table 1. Flow conditions

Before the sharp-fin calculations, a simple flat plate case with the same freestream conditions was run to calculate the undisturbed boundary layer properties. The domain for the flat plate case was 500 mm long, 100 mm high and 25 mm wide. Since SU2 v 4.2.0 did not have a built-in transition model, the coordinate system was shifted by a specific distance to match the boundary layer characteristics at a particular point. The momentum thickness Reynolds number (Re_θ) was matched with the experimental data at a particular streamwise location to determine that shift. The reason for specifically choosing Re_θ was that momentum thickness is known to be a robust measure for characterizing a turbulent boundary layer.[28,30] The details of the coordinate transformation are given in subsequent sections. The transformed coordinate system was used for the sharp-fin calculations with a domain 500 mm long, 100 mm high and 250 mm wide.

For meshing, the ANSYS ICEM-CFD package was used to construct an unstructured grid. The coarse

grid for the undisturbed boundary layer case consisted of 120 x 65 x 5 cells. The initial grid spacing off the wall was kept at $\Delta y^+ = 0.1$ to sufficiently resolve the thin viscous sub-layer and capture the corresponding boundary layer profile accurately. The corresponding dimensional distance of the first grid point from the wall is 4×10^{-7} m. Clustering of cells was done in the wall normal direction and near the flat plate leading edge with a stretching ratio of 1.2. The medium and fine grids were constructed from the coarse grid using a grid refinement ratio of 2. The medium grid on an x–y plane for the flat plate case is shown in Fig. 2(a).

A supersonic inlet condition was set on the plane $x = 0.1\,\text{m}$, where all the primitive variables were specified. Supersonic outlet conditions were imposed on the spanwise boundaries $z = 0\,\text{m}$ and $z = 0.025\,\text{m}$ as well as on the upper boundary at $y = 0.1\,\text{m}$. A symmetry plane was created upstream of the flat plate leading edge ($-0.1\,\text{m} < x < 0\,\text{m}$) to induce a spatially developing turbulent boundary layer. A no-slip isothermal wall was set on the surface at $y = 0\,\text{m}$ with $T_w = 300\,\text{K}$.

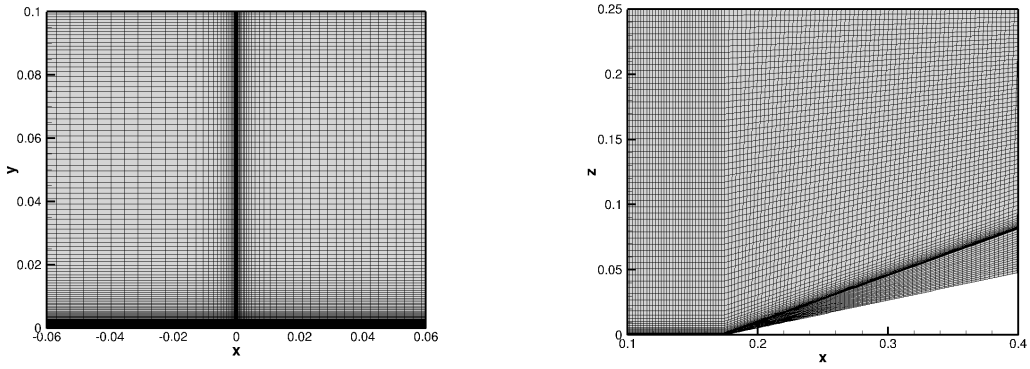

(a) Flat plate

(b) Sharp fin

Figure 2. Selected planes from medium grids for flat plate and sharp-fin geometries

A similar approach was taken for generating grids for the sharp-fin geometry. The coarse grid consisted of 212 x 65 x 100 cells with the same value of Δy^+ in Table 1. The medium and fine grids were constructed from the coarse grid using a grid refinement ratio of 2. Clustering of cells was done in the wall-normal direction and along the inviscid shock wave angle $\phi = 21.1°$ to align the grid with the inviscid shock trace. Shock aligned grids are highly desirable, especially in high Mach number flows, to prevent amplification of numerical error generated at the strong shock wave.[31] The top view of a medium grid on an x–z plane is shown in Fig. 2(b).

Boundary conditions for this domain were similar to the flat plate case. A supersonic inlet with the values of primitive variables were defined at $x = -0.1\,\text{m}$. Supersonic outlet conditions were specified on the spanwise planes $z = 0$ $(x < 0.17445)\,\text{m}$, $z = 0.25\,\text{m}$ as well as on the upper boundary $y = 0.1\,\text{m}$. A symmetry plane was created at $-0.1\,\text{m} < x < 0\,\text{m}$ to induce a spatially developing turbulent boundary layer. A no-slip isothermal wall was set on the flat plate surface at $y = 0\,\text{m}$ and the fin surface (along the spanwise plane $z = 0\,\text{m}$, $x > 0.17445\,\text{m}$) with $T_w = 300\,\text{K}$. For the case with application of plasma actuators, the same grid was used but it was resolved near the source term location, and the wall boundary condition was changed from no-slip isothermal to no-slip adiabatic.

II.B. Numerical method

Calculations were carried out using the SU2 code developed by the Aerospace Design Lab (ADL) at Stanford University.[32] It is currently under active development by many international collaborators.[x] SU2 is an open source unstructured finite volume solver implemented with object-oriented class architecture in C++ and high level Python scripts. The SU2 suite consists of several modules which are C++ executables, each designed for a specific task. The most commonly used module is SU2_CFD, which is responsible for solving a wide variety of partial differential equations (PDE's) such as Euler, Navier-Stokes, and RANS equations. The compressible RANS equations used by SU2 are as follows,[32]

[x]http://su2.stanford.edu/develop.html

$$\frac{\partial \rho}{\partial t} + \nabla.(\rho \vec{v}) = 0 \tag{1}$$

$$\frac{\partial (\rho \vec{v})}{\partial t} + \nabla.(\rho \vec{v} \otimes \vec{v} + p\bar{\bar{I}} - \bar{\bar{\tau}}) = \vec{q}_{\rho \vec{v}} \tag{2}$$

$$\frac{\partial (\rho E)}{\partial t} + \nabla.(\rho E \vec{v} + p\vec{v}) - \nabla.(\bar{\tau}.\vec{v} + \mu_{tot} c_p \nabla T) = q_{\rho E} \tag{3}$$

In the above equations, $\mu_{tot} = \mu + \mu_t$ is the total dynamic viscosity as the sum of molecular and turbulent viscosity and $\vec{q}_{\rho \vec{v}}$, $q_{\rho E}$ are the source terms to model the plasma actuator. To calculate the primitive variables, the internal energy equation, perfect gas law, and Sutherland's law of viscosity (to account for variation with temperature) are used,

$$p = (\gamma - 1)\rho \left(E - \frac{\vec{v}.\vec{v}}{2} \right) \tag{4}$$

$$T = \frac{p}{\rho R} \tag{5}$$

$$\mu = \mu_0 \left(\frac{T}{T_0} \right)^{3/2} \left(\frac{T_0 + S}{T + S} \right) \tag{6}$$

The unknown Reynolds stresses are modeled using the Boussinesq approximation and the kinematic eddy viscosity is calculated by the one equation Spalart-Allmaras (SA) turbulence model.[33]

The inviscid fluxes were discretized using the Roe scheme[34] for flat plate boundary layer calculations and AUSM flux splitting scheme[35–37] for flows involving sharp gradients and complex physics. A higher order reconstruction for second order accuracy was implemented for upwind schemes with the Venkatakrishnan[38] limiter switched on. The derivatives required for the evaluation of the viscous fluxes were calculated using the Green-Gauss theorem and piecewise reconstruction method was used for the source terms.[32] The solutions were marched to steady state using first order implicit Euler time-stepping with a CFL number of 0.1. The linear system was solved using the Generalized Minimal Residual Method (GMRES) with the multigrid level set to 0.

II.C. Source term implementation

Based upon previous computational studies by Bisek and Poggie[9,21] and Atkinson and Poggie,[17] the plasma actuator was modeled semi-empirically as a heat source and magnetic bodyforce term in the energy and momentum equations respectively. The mathematical expression for the source term is,

$$\begin{aligned} S(x,y,z) &= \frac{1}{K} \exp \left[- \left(\frac{x - x_c}{a} \right)^2 - \left(\frac{y - y_c}{b} \right)^2 - \left(\frac{z - z_c}{c} \right)^2 \right] \\ \vec{q}_{\rho \vec{v}} &= \vec{F} S(x,y,z) \\ q_{\rho E} &= \left(Q + \vec{F}.\vec{v} \right) S(x,y,z) \end{aligned} \tag{7}$$

In Eq.(7), $\vec{F} = (\vec{I} \times \vec{B})w$, $Q = VI$, K is a scaling factor, (x_c, y_c, z_c) are the coordinates of the centroid of the actuator, and a, b, c are its characteristic length scales in the streamwise, wall-normal and spanwise direction respectively. The source term is scaled such that,

$$\iiint_{-\infty}^{\infty} S(x,y,z)\, dx\, dy\, dz = 1 \tag{8}$$

$$K = \pi^{3/2}\, a\, b\, c \tag{9}$$

K has the units of volume (m^3), and therefore from Eq.(8), S has the units of reciprocal of volume (m^{-3}). Hence, the source term expressions in Eq.(7) have the units of force or power per unit volume.

A hemispherical bump was designed by maintaining the y-centroid location at 0 (on the wall) and keeping the length scales a, b and c equal in value. The length scales were adjusted such that the hemispherical bump was well within the viscous boundary layer. For the study, a hemispherical shape was considered by setting $a = b = c = w$. To validate the implementation of the source term, an energy balance exercise using inviscid Euler calculations of the source term placed in a 2D box were carried out. The rectangular domain was 3 m long and 1 m wide, and consisted of 300 x 100 cells. The source term was positioned at the center. The % error between the difference of total enthalpies at the outlet and inlet, and the power input to the source term was found to be 2.6%, which is acceptable for the mesh size used.

III. Results

This section is divided into three parts. In the first section, the results of undisturbed boundary layer case are presented. In the next section, the sharp fin flowfield is discussed in detail and computational results are compared with experimental data. The concluding section describes the effect of plasma actuator on the sharp-fin flowfield and results are compared with the baseline case.

III.A. Incoming boundary layer

This section delves into the properties of the incoming turbulent boundary layer. The numerically-implemented source term is also tested on a flat plate turbulent boundary layer and the effects of the consequent thermal perturbation are investigated briefly. The thermal perturbation created by the source term creates a virtual hemispherical bump which leads to a pair of counter-rotating vortices in its wake.

III.A.1. Undisturbed boundary layer

Plots of boundary layer parameters such as displacement thickness, momentum thickness, boundary layer thickness, and skin-friction coefficient are compared to the experimental data by Schülein.[29]

The compressible boundary layer displacement and momentum thickness are calculated using the following expressions,

$$\delta^* = \int_0^\infty \left(1 - \frac{\rho(y)u(y)}{\rho_\infty u_\infty}\right) dy \tag{10}$$

$$\theta = \int_0^\infty \frac{\rho(y)u(y)}{\rho_\infty u_\infty}\left(1 - \frac{u(y)}{u_\infty}\right) dy \tag{11}$$

The plots of evolution of these three quantities and variation of skin friction coefficient are shown in Fig. 3 along with the corresponding experimental data.

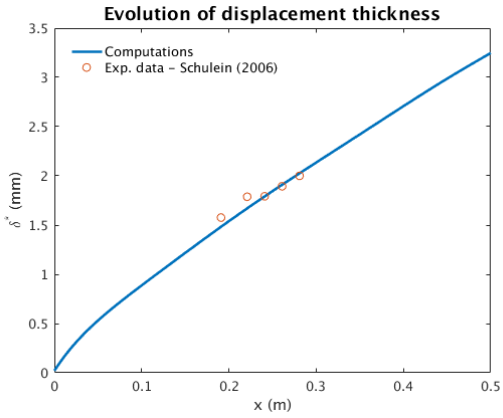

(a) Displacement thickness

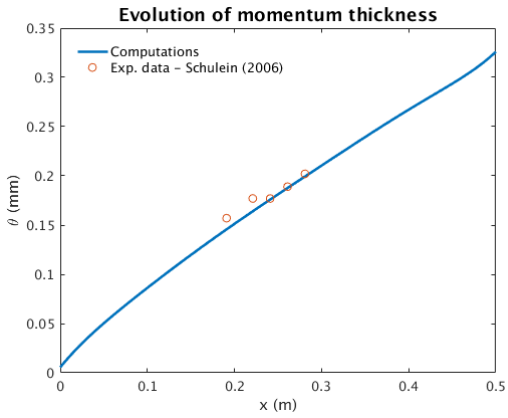

(b) Momentum thickness

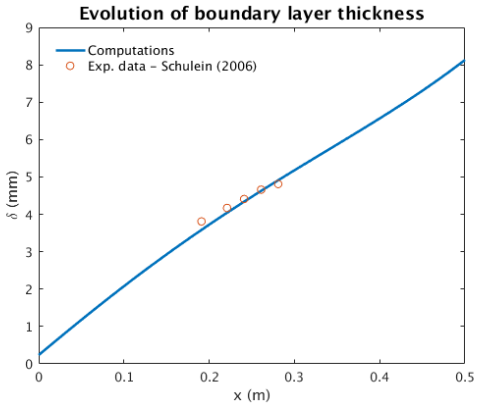

(c) Boundary layer thickness

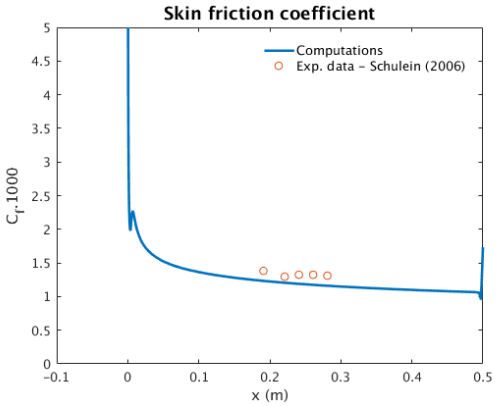

(d) Skin friction coefficient

Figure 3. Undisturbed boundary layer properties (for medium grid)

The boundary layer thickness δ is defined as the wall normal location where $u(y) = 0.995u_\infty$. Equations (10)–(11) were integrated numerically using the trapezoidal method to obtain the values at each streamwise station. To account for the absence of a transition model, the experimental coordinate system was shifted upstream by 75.05 mm to match the boundary layer properties at the fin leading edge. From Fig. 3, it can be observed that the computational results agree well with the experimental data of Schülein.[29]

To collapse the compressible boundary layer profile on the incompressible law of the wall, the Van-Driest transform was used to account for density variations.

$$u^+_{VD} = \int_0^{u^+} \left(\frac{\overline{\rho}}{\rho_w}\right)^{1/2} du^+ \tag{12}$$

The transformed velocity profile is shown below Fig. 4.

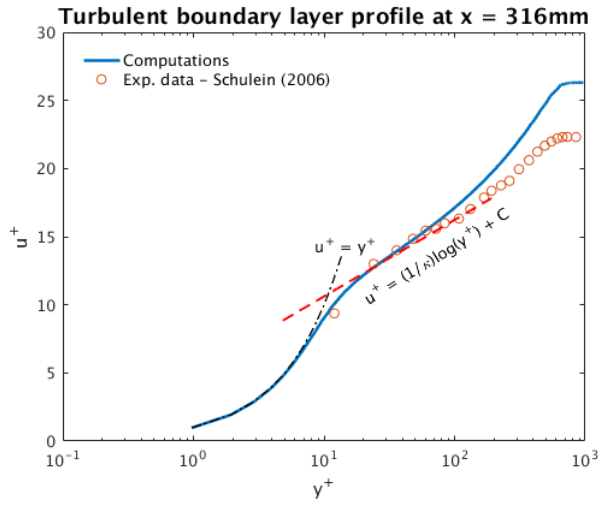

Figure 4. Van-Driest transformed velocity profile at x = 316 mm

The Van-Driest transform works well for adiabatic flows, but breaks down when the wall is either heated or cooled by the flow. The current undisturbed boundary layer case consisted of an isothermal wall maintained at a temperature of 300 K while the corresponding adiabatic wall temperature was about $T_{aw} = 373$ K, indicating a cold wall. Hence there was significant heat transfer, which led to deviation from the incompressible profile. For the current case, the Van-Driest transformed velocity profile is plotted in Fig. 4 and compared with the transformed experimental data by Schülein.[29] The collapsed profile agrees well in the viscous sublayer where $u^+ = y^+$, but shows an upward shift in the log-law intercept, which is consistent with the results obtained for a cooled wall by Trettel and Larsson.[39]

III.A.2. Boundary layer with source term

Based on the computations by Yan and Gaitonde,[40–42] computations with the source term placed in a flat plate turbulent boundary layer were carried out in the absence of a bodyforce. The source term was located at $x = 0.27745\,\text{m}$, $y = 0\,\text{m}$ and $z = 0.0125\,\text{m}$. To avoid high temperature gradients at the wall, the boundary condition there was changed from no-slip isothermal to no-slip adiabatic wall, as mentioned in Sec. II.A. Based on Eq.(7) in Sec. II.C, the thermal bump is hemispherical in shape with a characteristic Gaussian distribution. The mean streamwise vorticity contours (ω_x) are shown in Fig. 5, with the coordinates non-dimensionalized by the boundary layer thickness.

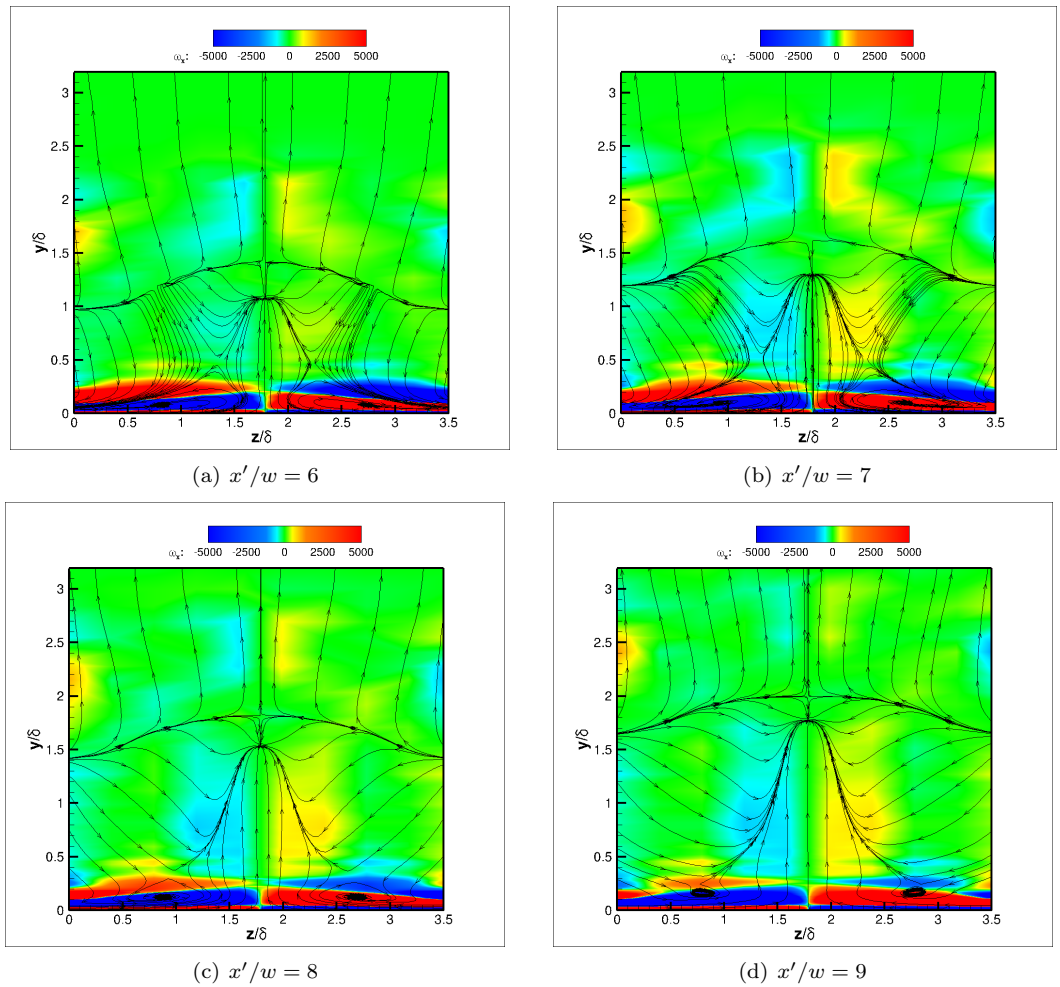

(a) $x'/w = 6$ (b) $x'/w = 7$

(c) $x'/w = 8$ (d) $x'/w = 9$

Figure 5. Flowfield in presence of source term, downstream view of streamwise vorticity with sectional streamlines

As a result, this "thermal bump" spawns a pair of counter-rotating vortices in its wake, around $6w$ downstream of its location. The vortices are lifted off from the surface and decay around $9w$ downstream of the bump. A way to visualize this is by looking at the vorticity equation. Joule heating causes local variation in pressure and density, which leads to non-aligned density and pressure gradients. Consequently, the lower density fluid will be accelerated more than the higher density fluid, generating vorticity. This phenomenon is represented by the baroclinic torque in the vorticity equation as $(\nabla\rho \times \nabla p)/\rho^2$. The flow structures in the wake of a hemispherical thermal bump are different from a solid hemispherical bump because the former is "penetrable".[40] A shock is associated with the hemispherical bump which weakens downstream to form a Mach wave.

III.B. Sharp fin results

Following the validation of the upstream boundary layer with experimental data, the mean flowfield of the sharp-fin interaction was calculated. The results presented in this section are for the medium grid case. Analogous to the boundary layer calculations, the experimental coordinate system was moved upstream by 75.05 mm to account for absence of a transition model. The density contour obtained from computations at a streamwise plane $x = 342.45$ mm is shown in Fig. 6(a).

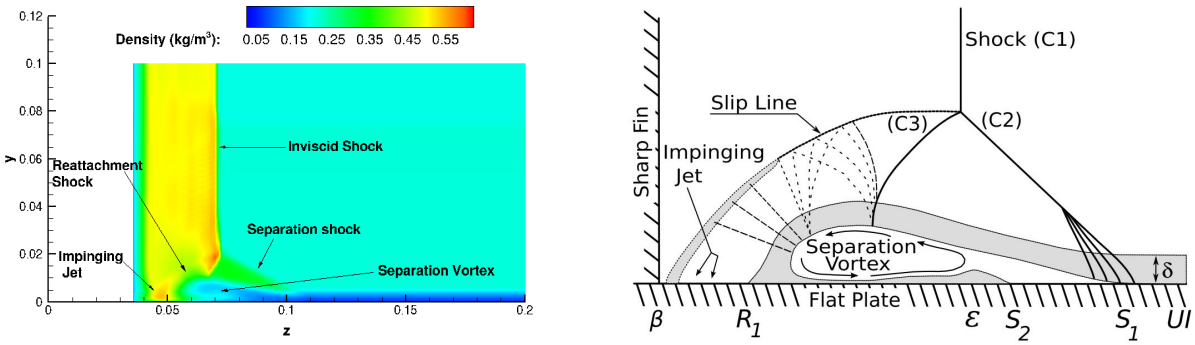

(a) Density Contours at x = 342.5mm

(b) Experimental flow structure (Leger et al.[28])

Figure 6. Comparison of flowfield

On comparing with the experimental flow structure in Fig. 6(b), it can be observed that all the physical flow features are captured by the RANS solution. The inviscid shock bifurcates into the separation and reattachment shock due to the presence of the separation bubble, forming a λ shock foot. Since the flow going through an inviscid shock will have a different velocity compared to the flow going through two weaker oblique shocks, a slip surface originates from the triple point and curves downwards, terminating at the junction of the sharp-fin and flat plate. After passing through the λ shock foot, the flow accelerates through expansion fans and reaches the surface as an impinging jet. These expansion fans reflect as compression waves, which coalesce to form "shocklets."[4] This is a classic Edney Type-IV interaction[43] which is characterized by amplified aerothermodynamic loads at the location of the impinging jet. A better representation of the three dimensional flowfield is shown in Fig. 7 by the iso-surfaces of density and surface streamtraces.

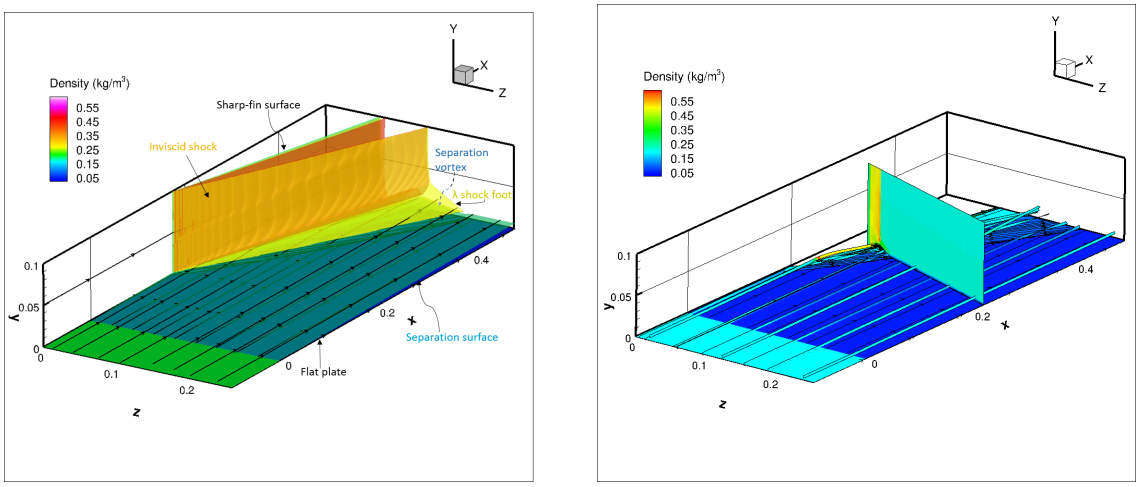

(a) Iso-surfaces of density

(b) Streamtraces on the plate surface

Figure 7. Three dimensional flowfield (Medium grid)

From Fig. 7(a), an the inviscid shock formed at the wave angle $\phi = 21.1°$, calculated from the weak oblique shock solution for $M_\infty = 5$ and turning angle $\alpha = 12°$, can be observed. The flow is deflected in the

direction parallel to the fin surface at the upstream influence line. At the separation line, it rolls up into a separation vortex which develops in thickness downstream. The impinging jet (not visible) is bounded by the slip surface on the left and the separation bubble on the right. Since the flow has a significant spanwise velocity, it does not re-attach after separation and continues in a helical trajectory downstream (shown in Fig. 7(b)) - forming an "open separation bubble" characteristic of 3D flowfields.[27]

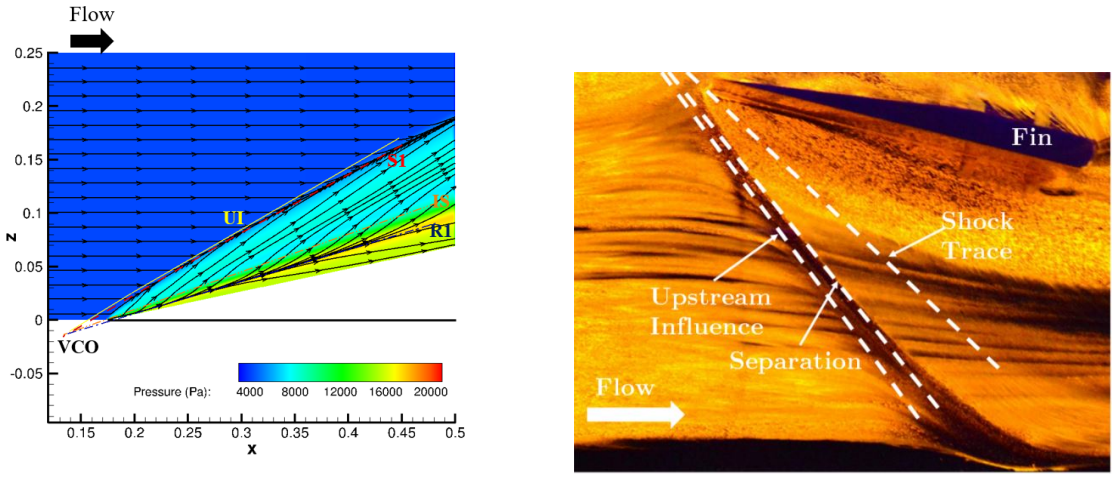

(a) Limiting Streamlines from computations

(b) Experimental result by Arora et al.[27]

Figure 8. Surface flow visualization

The conical symmetry exhibited by this interaction can be visualized in Fig. 8. In Fig. 8(a), the upstream influence line (UI), separation line (S1), inviscid shock trace (IS) and reattachment line (R1) converge at the virtual conical origin (VCO), close to the fin leading edge. The coordinates of the VCO were found to be at $(x, y, z) = (126.804, 0, -14)$ mm. The inception region can also be observed as a curved streamline which deviates from the separation line in the vicinity of the VCO. The surface flow features obtained from the computations agree qualitatively with the experimental results in Fig. 8(b).

The wall pressure profiles are shown in Fig. 9 and compared with the experimental data by Schülein[29] in normalized Cartesian coordinates. A grid convergence study is also shown in Fig. 9(b). The results for the medium grid agree within the experimental uncertainty. The pressure rise occurs in two stages which is typical for any shock wave boundary layer interaction. The initial pressure rise occurs due to upstream influence and the separation shock, and is followed by a pressure plateau. This pressure plateau is associated with the region under the separation vortex. The constant distribution of pressure is followed by a slight dip which recovers downstream to approach the inviscid value. Peak pressure is obtained at the location of the impinging jet.

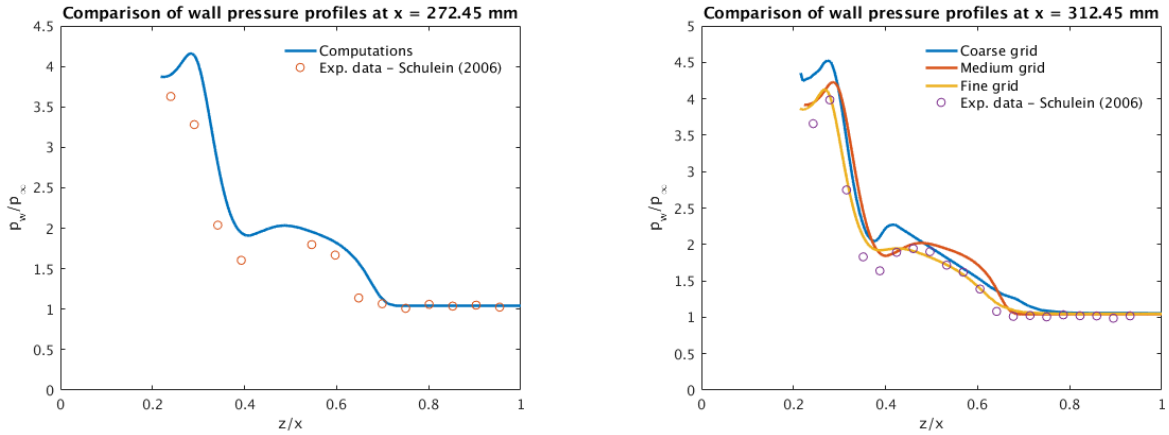

(a) x = 272.45 mm

(b) x = 312.45 mm

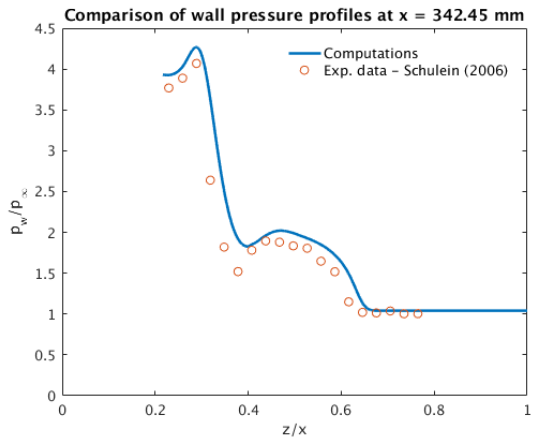

(c) x = 342.45 mm

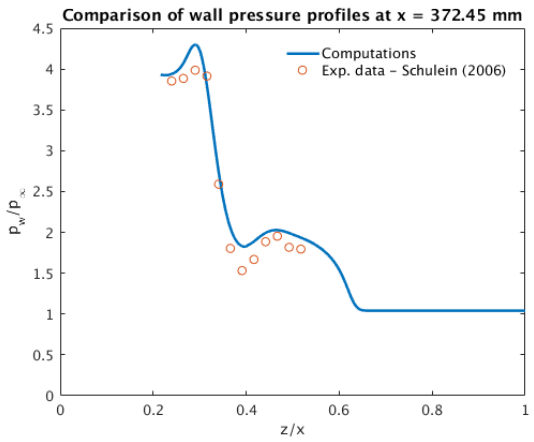

(d) x = 372.45 mm

Figure 9. Wall pressure profiles (Medium grid)

Wall heat transfer profiles from the computations are compared with experimental data in Fig. 10. Although the SA model predicted the wall pressure profiles with reasonable accuracy, a significant overestimation of heat transfer rate was observed. This result agrees with the computations done by Leger et al.,[28] who noted a 20% over-prediction of peak heat transfer rate for the SA-Catrix model of the US3D code.

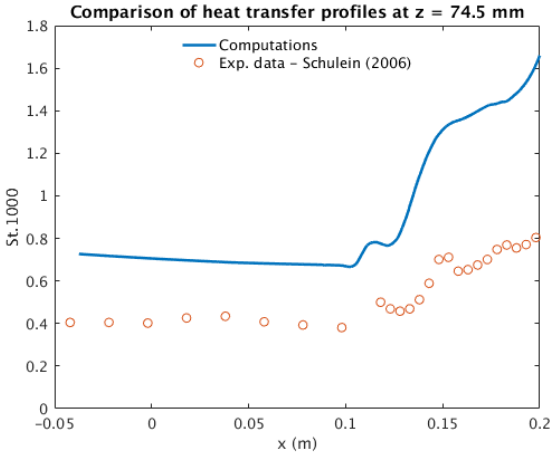

Figure 10. Wall heat transfer profile at z = 74.5 mm

Due to the conical behavior of the flowfield, a spherical coordinate system is a natural choice to plot the trend of physical quantities. Arora and Alvi[27] determined the scaling that collapsed wall pressure profiles associated with different free-stream conditions onto a single curve but approximately same interaction strength, plotted in spherical coordinates. The magnitude of the interaction strength is determined by the parameter - $M_\infty \sin\phi$. The non-dimensional angular extent $(\beta - \phi)/\mu^*$, where μ^* is the Mach angle, accounts for the freestream Mach number, angle of attack of the fin, and sweepback caused by freestream Mach number. The wall pressure was initially normalized using the freestream value - which did not collapse the peaks.

A new scaling variable for pressure $(p_w - p_\infty)/(p_{max} - p_\infty)$ is used here which resolves this issue. The wall pressure profile extracted at an arbitrary location $r = 0.21$ m, is plotted against the azimuthal angle β. The experimental data from Garg and Settles[44] with $M_\infty = 3$ and $\alpha = 20°$ are used to judge the performance of the scaling. As observed from Fig. 11, the suggested scaling collapses the two plots of approximately same interaction strength onto a single profile. The peaks as well as pressure plateau region coincide very well with a slight deviation at the "pressure dip" location.

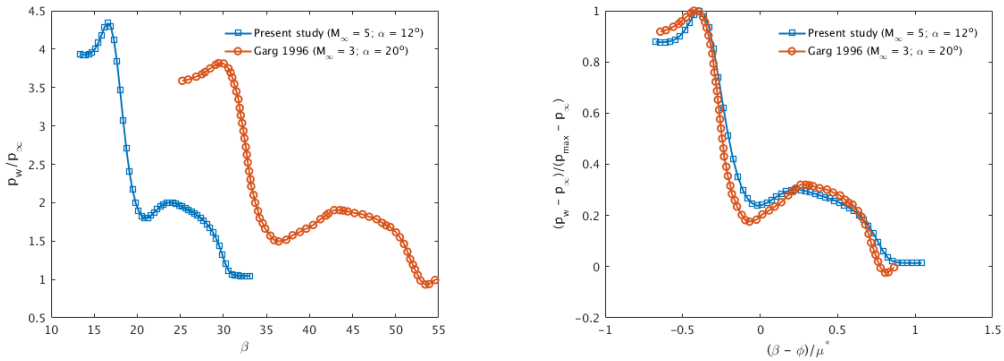

(a) Unscaled wall pressure

(b) Scaled wall pressure

Figure 11. Scaling of wall pressure profiles

III.C. Flow control

On validating the computational results of the baseline case with experiments, the effect of plasma actuators on the three dimensional flowfield is explored in this section. Two different modes of plasma actuation are investigated: heat alone and a combination of heat and bodyforce. The voltage and current values were taken from experiments conducted by Kalra et al.[19] The actuator was placed along the upstream influence line and the bodyforce was oriented along the direction parallel to the fin surface.

III.C.1. Heat alone

For the first case, effect of volumetric energy deposition on the flowfield was investigated without the presence of bodyforce. It was assumed that all the energy input to the actuator goes entirely into heating the flow. The coordinates of the centroid of the actuator were $(x_c, y_c, z_c) = (297.2, 0, 90.1)$ mm and the concomitant characteristic length scale was $w = 2\,\text{mm}$, to place it within the boundary layer.

Experiments on flow control using pulsed plasma jets by Greene et al.,[24] determined that the optimum position for placing the jets was around 1.5δ upstream of a compression ramp corner. For distances greater than 3δ, the positive effects of jets diminished abruptly; which indicates that mixing of the boundary layer by the vortices decays rather rapidly. The authors asserted that this result was a consequence of a "tradeoff" between two phenomena: the generation of streamwise vorticity that enhances the net momentum of the boundary layer, and the dissipative heat that makes the boundary layer susceptible to separation by increasing its shape factor. Based on these results, the position of the actuator was chosen such that it was 1.5δ away from the separation line. The power input to the actuator was $Q = IV = 500\,\text{W}$, which corresponds to a potential drop of 5 kV and a current of 100 mA. According to Kalra et al.,[18,19] for current values exceeding 250 mA, the negative effect of heating overshadows the positive effects. The corresponding non-dimensional power $\tilde{Q} = Q/(\rho_\infty u_\infty^3 \delta_\circ^2) = 0.39$, where $\delta_\circ$ is the boundary layer thickness at the fin leading edge.

As mentioned earlier in Sec. II.A, the wall boundary condition was changed from no-slip isothermal to no-slip adiabatic for the actuator calculations. In doing so, high temperature gradients were prevented at the actuator location which otherwise would have precluded convergence. To be consistent in our approach, a medium grid for the baseline case was run with an adiabatic no-slip condition at the wall for the purposes of comparison. Henceforth, the pressure and skin-friction plots will be plotted in spherical coordinates to observe the conical nature of the flowfield. The limiting streamlines plot for the flow control case is shown in Fig. 12, and compared with baseline case.

The location of the actuator can be identified as a spot of high pressure in Fig. 12(b). The separation line conformed to the actuator shape as it forked at the leading edge and merged some distance downstream. The interaction footprint remained relatively unchanged with a distinct reattachment line. Hence it is reasonable to assume that the property of conical similarity is preserved after the application of flow control, except in the vicinity of the actuator, where apparent bow shocks would alter the trend of wall pressure profiles. The separation extent is increased for the flow control case, which is indicated by a higher value of the z-intercept, z_{sep}. This value is defined as the intercept obtained at the intersection point of the separation line and the

exit of the domain at $x = 0.5\,\text{m}$. In Fig. 12(a), $z_{sep} \approx 0.195\,\text{m}$ for the baseline case, and for the flow control case in Fig. 12(b), $z_{sep} \approx 0.214\,\text{m}$. This occurs as a result of heating the flow, which rarifies the fluid around the actuator location. Hence to maintain the same mass flux, the separation bubble must expand.[23]

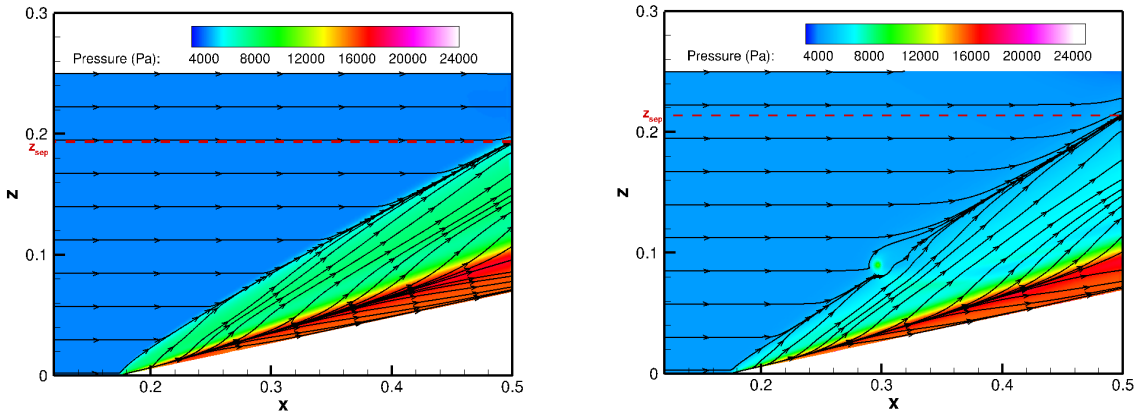

(a) Basline case (b) Flow control (heat alone)

Figure 12. Comparison of surface flow features (Medium grid)

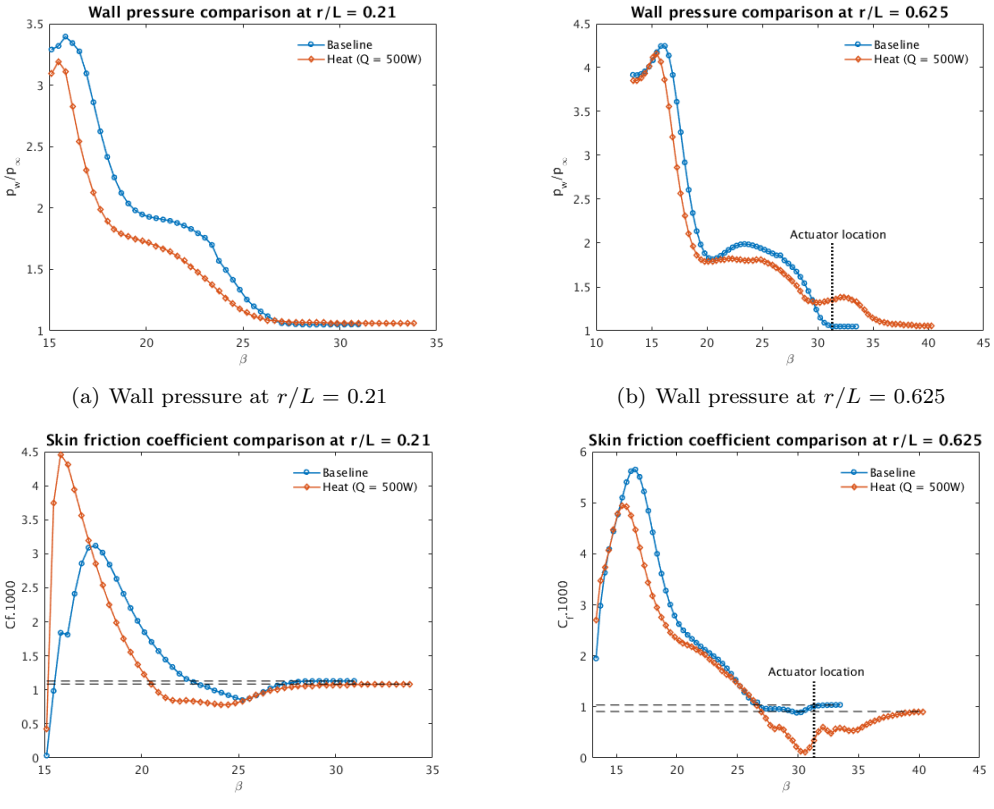

(a) Wall pressure at $r/L = 0.21$ (b) Wall pressure at $r/L = 0.625$

(c) Skin-friction coefficient at $r/L = 0.21$ (d) Skin-friction coefficient at $r/L = 0.625$

Figure 13. Comparison of wall quantities - Heat alone (Medium grid)

The locations selected for extracting wall pressure and skin-friction data were motivated by Arora et al.[27] The locations $r/L = 0.21$ and $r/L = 0.625$ correspond to the inception region and farfield region (in

the vicinity of the actuator location) respectively. From 12(b), it is discernible that coordinate of the VCO has changed on implementing the source term. Also, due to absence of a distinct separation line, it was difficult to determine the coordinates of new VCO with certainty. Therefore, for convenience of comparison, the radial distance r was measured from the original VCO determined for the baseline case.

Some useful insights about the effect of plasma actuator control can be obtained from Fig. 13. The wall pressure profiles in Fig. 13(a) and Fig. 13(b) show a decreased strength of the λ shock foot. The extent of upstream influence does not seem to be affected significantly as the pressure plateau region is similar to the baseline case. The reduction in peak pressure value is subtle at $r/L = 0.625$, but more pronounced at $r/L = 0.21$ which lies in the inception region. Also, a small increment in pressure can be observed near the actuator location due to a bow shock associated with it.

Increase in separation extent is evident from the skin-friction plots in Fig. 13(c) and Fig. 13(d). The minimum skin-friction coefficient always remained positive, which reinforces the point of view of an "open" separation bubble. Also, the movement of pressure and skin-friction coefficient peaks to a smaller azimuthal angle indicates shifting of the impinging jet towards the fin-plate junction with application of flow control. The corresponding magnitude of the displacement was found to be $\Delta\beta \approx 1.08°$. The disparity in wall profiles within the inception region and the farfield region is consistent as peak skin friction coefficient increases in the former and decreases in the later case. This behavior is reasonable since the conical similarity does not apply in the inception region. The reason for decrease in the peak skin-friction coefficient can be attributed to increase in the boundary layer shape factor due to heating. Another cause might be the turning of the flow through weaker expansion fans, leading to a lower terminal velocity of the impinging jet.

III.C.2. Heat + Bodyforce

An external magnetic field was applied to the plasma actuator to create a magnetic bodyforce aligned parallel to the fin surface in the flow direction. To simulate this effect, respective source terms were added in the momentum equations in addition to the one previously present in the energy equation. The magnetic field was chosen to match the experiments of Kalra et al.,[19] where its magnitude was 3 T. For a current of 100 mA, the force generated was $|\vec{F}| = IBl = 6 \times 10^{-4}$ N, where $l = w = 2$ mm. The components in the streamwise direction $F_x = |\vec{F}| \cos\alpha \hat{i}$ N and in the spanwise direction $F_z = |\vec{F}| \sin\alpha \hat{k}$ N. The wall normal component F_y was set to be 0 N.

The limiting streamlines for the bodyforce case is compared with the baseline case in Fig. 14. No significant change the flowfield is observed as compared to the "heat alone" case in Fig. 12(b). A slightly higher value of the z-intercept ($z_{sep} \approx 0.22$ m) for this case as compared to the "heat alone" case ($z_{sep} \approx 0.214$ m) indicates increased separation extent. Similar trends such as bifurcation of the separation line on encountering the actuator, increased separation extent, and localized high pressure at the actuator location due to bow shocks are observed.

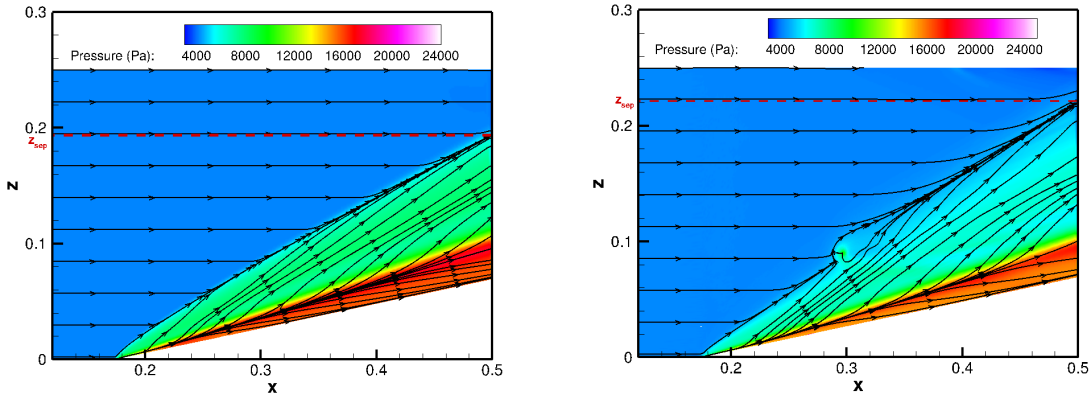

(a) Basline case (b) Flow control (heat + bodyforce)

Figure 14. Comparison of surface flow features (Medium grid)

The wall pressure and skin friction coefficient data is extracted at the same r/L locations discussed in Sec. III.C.1. Also, the coordinates of VCO are adopted from the baseline case.

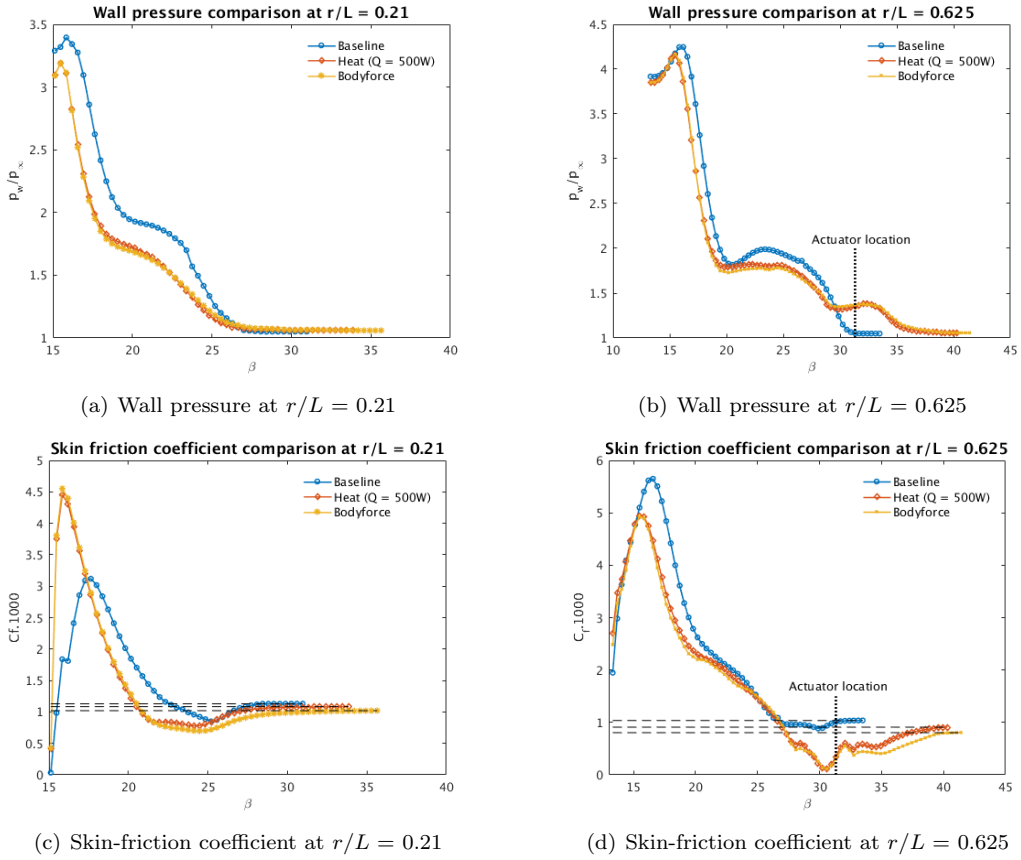

(a) Wall pressure at $r/L = 0.21$

(b) Wall pressure at $r/L = 0.625$

(c) Skin-friction coefficient at $r/L = 0.21$

(d) Skin-friction coefficient at $r/L = 0.625$

Figure 15. Comparison of wall quantities - Heat + Bodyforce (Medium grid)

The profiles in Fig. 15 are almost indistinguishable from the "heat alone" case discussed in Sec. III.C.1, with similar divergence noted for plots in the inception region and farfield region. This suggests that the interaction strength is too high for bodyforce to have any significant effect. A small variation in the skin friction coefficient plots is observed on applying the bodyforce. This confirms that the source term is indeed functioning by changing the force balance between the separation bubble and wall shear stress on the surface. Also, the impinging jet is displaced from its original location by the same magnitude ($\Delta\beta \approx 1.08°$) as in the "heat alone" case. Nevertheless, the dominant effect was still found to be Joule heating due to the actuator. Therefore, if a single actuator is used, unrealistically high values of current and magnetic field might be required to generate a force strong enough to affect the flowfield.

To test this hypothesis, a case with highest practical values of current and magnetic field, which correspond to 10 A and 10 T respectively, was simulated. The corresponding force generated was $|\vec{F}| = IBl = 2\times10^{-1}$ N, which was three orders of magnitude higher than the previous case. To maintain a constant power input Q to the actuator, the potential drop was considered to be 50 V, which was within the experimental range of Kalra et al.[19] The resulting pressure and skin-friction coefficient plots are shown below in Fig. 16. Since the interaction footprint is similar to the one in Fig. 14(b), for brevity, it is not shown here.

The plots indicate no substantial effect on the flow-field. In the inception region at $r/L = 0.21$, the peak value of skin-friction coefficient increases progressively with the energy input to the actuator, accompanied by a higher separation extent. The corresponding pressure plots show a small drop in the strength of the λ shock foot. The pressure plots at $r/L = 0.625$ follow a similar trend. The strength of the bow shock associated with the actuator is found to increase in strength with more power input. A local peak value of skin-friction coefficient near the actuator location at $r/L = 0.625$, indicates possible reattachment of the flow before separating again. The impinging jet experiences a similar displacement from its original location ($\Delta\beta \approx 1.08°$), as in the previous cases.

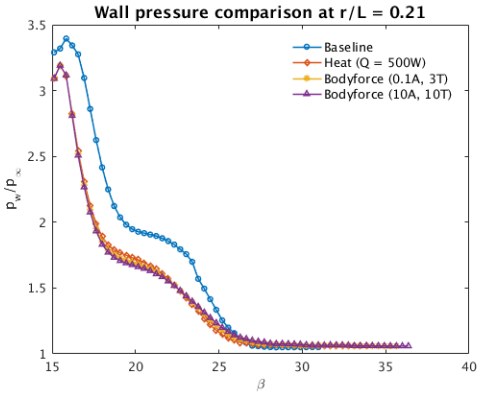

(a) Wall pressure at $r/L = 0.21$

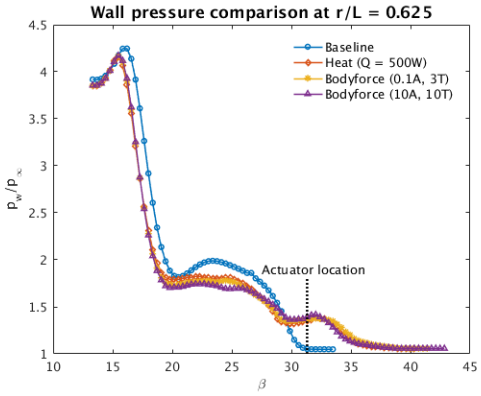

(b) Wall pressure at $r/L = 0.625$

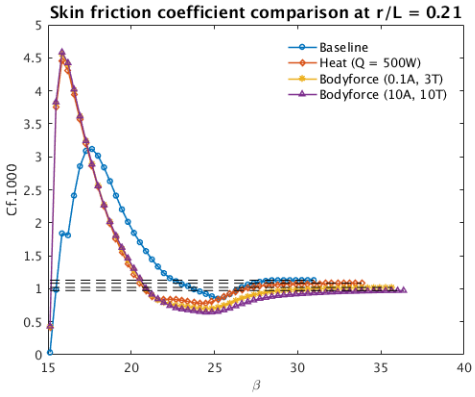

(c) Skin-friction coefficient at $r/L = 0.21$

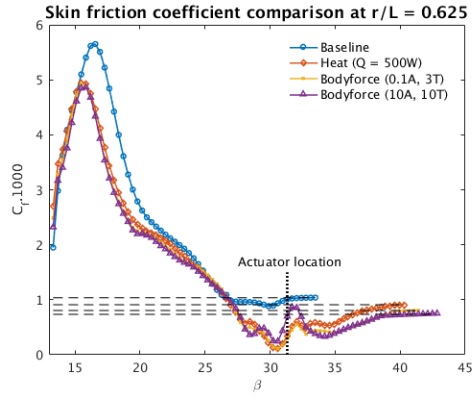

(d) Skin-friction coefficient at $r/L = 0.625$

Figure 16. Comparison of wall quantities - Unrealistic case (Medium grid)

IV. Conclusions

A RANS study was performed using the SU2 code for the sharp-fin/flat-plate geometry, for the freestream conditions used in the experiments by Schülein.[29] On comparing with experimental data, the SA turbulence model showed reasonable accuracy in predicting the behavior of wall pressure profiles and capturing flow features of the resulting three-dimensional interaction. However, a significant variation in wall heat transfer profile was observed from experimental data. The code was modified to include source terms in the momentum and energy equations to model a plasma actuator semi-empirically. An energy balance test was performed to check the implementation of source term and its effects on a flat plate turbulent boundary were investigated. A pair of counter-rotating vortices was observed in the wake of the "thermal bump," which decay after a specific distance downstream. The application of plasma actuator on the sharp-fin/flat-plate flowfield was done using two modes: heat alone and a combination of heat and bodyforce. The dominant effects of plasma actuation were increased separation extent, decreased strength of λ shock foot and reduction in peak skin friction coefficient - which is of engineering significance. With the experimental parameters, the resulting bodyforce was too weak to alter the interaction significantly. To test if unrealistic values of current and magnetic field were required to create a significant impact on the flow-field, a case with $I = 10\,\mathrm{A}$ and $B = 10\,\mathrm{T}$ was simulated. No significant change in the flow-field was observed, with the exception of brief flow reattachment near the actuator location with application of flow control. Interestingly, the impinging jet was shifted by the same magnitude from its original location, irrespective of the energy input to the actuator. Assuming the same VCO for the flow control cases might be a reason for this phenomenon. Hence, determination of a unique VCO corresponding to a particular flow control case is necessary.

Since implementation of a single actuator demands an unfeasible energy input, a case with multiple actuators placed at equal intervals along the upstream influence line would be a promising approach. Also, the placement of the actuators is not trivial and warrants a detailed parametric study to determine its

optimum location. In this computation, it was assumed that all the power input to the actuator goes into heating the flow. In reality, 90% of the heat goes into excitation of N_2 gas (primarily vibrational modes) in air while only the remaining 10% goes into heating of the flow.[18,19] Considering vibrational relaxation time scales, the lost vibrational energy never returns. Nevertheless, the purpose of this study was to initiate investigation of plasma flow control in essentially three-dimensional flowfields, which in the past, has been limited to two-dimensional interactions exhibited by compression ramps.

Acknowledgments

This work was funded in part by the AFOSR Grant FA9550-17-1-0153, monitored by I. Leyva. The authors are grateful to Dr. Timothy Leger for helping us obtain Schülein's experimental data for computational validation. Also, the staff of Purdue's Rosen Center for Advanced Computing (RCAC) is appreciated for consistent maintenance of the community clusters and ensuring its smooth operation.

References

[1]D. Gaitonde. Progress in shock wave/boundary layer interaction. *Progress in Aerospace Sciences*, 72:80–99, 2015.

[2]J. Green. Interactions between shock waves and turbulent boundary layers. *Progress in Aerospace Sciences*, 11:235IN9261–260IN10340, 1970.

[3]J-P. Dussauge, P. Dupont, and J-F. Debive. Unsteadiness in shock wave boundary layer interactions with separation. *Aerospace Science and Technology*, 10:85–91, 2006.

[4]H. Babinsky and J. Harvey. *Shock wave-boundary-layer interactions*, volume 32. Cambridge University Press, 2011.

[5]H. Babinsky, N. Makinson, and C. Morgan. Micro-vortex generator flow control for supersonic engine inlets. In *45th AIAA Aerospace Sciences Meeting and Exhibit*, page 521, 2007.

[6]H. Holden and H. Babinsky. Effect of microvortex generators on seperated normal shock/boundary layer interactions. *Journal of Aircraft*, 44(1):170–174, 2007.

[7]H. Babinsky and H. Ogawa. Shock wave-boundary layer interaction control for wings and inlets. *Shock Waves*, 18(2):89–96, 2008.

[8]J. Lin. Review of research on low-profile vortex generators to control boundary-layer separation. *Progress in Aerospace Sciences*, 38(4):389–420, 2002.

[9]N. Bisek, D. Rizzetta, and J. Poggie. Plasma control of a turbulent shock boundary-layer interaction. *AIAA Journal*, 51(8):1789–1804, 2013.

[10]I. Girgis, S. Macheret, G. Brown, R. Miles, and M. Shneider. Creation of steering moments in supersonic flow by off-axis plasma heat addition. In *40th AIAA Aerospace Sciences Meeting & Exhibit*, page 129, 2002.

[11]I. Girgis, M. Shneider, S. Macheret, G. Brown, and R. Miles. Steering moments creation in supersonic flow by off-axis plasma heat addition. *Journal of spacecraft and rockets*, 43(3):607–613, 2006.

[12]J. Shang, D. Gaitonde, and G. Updike. Modeling magneto-aerodynamic actuator for hypersonic flow control. In *35th AIAA Plasmadynamics and Lasers Conference*, page 2657, 2004.

[13]J. Shang, R. Kimmel, J. Menart, and S. Surzhikov. Hypersonic flow control using surface plasma actuator. *Journal of Propulsion and Power*, 24(5):923–934, 2008.

[14]J. Shang. *Computational electromagnetic-aerodynamics*. John Wiley & Sons, 2016.

[15]G. Updike, J. Shang, and D. Gaitonde. Hypersonic separated flow control using magneto-aerodynamic interaction. In *43rd AIAA Aerospace Sciences Meeting and Exhibit*, page 164, 2005.

[16]D. Gaitonde. High-speed magnetohydrodynamic flow control analyses with three-dimensional simulations. *Journal of Propulsion and Power*, 24(5):946–961, 2008.

[17]M. Atkinson, J. Poggie, and J. Camberos. Control of separated flow in a reflected shock interaction using a magnetically-accelerated surface discharge. *Physics of Fluids*, 24(12):126102, 2012.

[18]C. Kalra, M. Shneider, and R. Miles. Numerical study of boundary layer separation control using magnetogasdynamic plasma actuators. *Physics of Fluids*, 21(10):106101, 2009.

[19]C. Kalra, S. Zaidi, R. Miles, and S. Macheret. Shockwave–turbulent boundary layer interaction control using magnetically driven surface discharges. *Experiments in fluids*, 50(3):547–559, 2011.

[20]S. Macheret, M. Shneider, and R. Miles. Scramjet inlet control by off-body energy addition: a virtual cowl. *AIAA Journal*, 42(11):2294–2302, 2004.

[21]N. Bisek, I. Boyd, and J. Poggie. Numerical study of plasma-assisted aerodynamic control for hypersonic vehicles. *Journal of Spacecraft and Rockets*, 46(3):568–576, 2009.

[22]V. Narayanaswamy, L. Raja, and N. Clemens. Control of unsteadiness of a shock wave/turbulent boundary layer interaction by using a pulsed-plasma-jet actuator. *Physics of Fluids*, 24(7):076101, 2012.

[23]N. Webb, C. Clifford, and M. Samimy. Control of oblique shock wave/boundary layer interactions using plasma actuators. *Experiments in fluids*, 54(6):1545, 2013.

[24]B. Greene, N. Clemens, P. Magari, and D. Micka. Control of mean separation in shock boundary layer interaction using pulsed plasma jets. *Shock Waves*, 25(5):495–505, 2015.

[25]N. Arora, M. Ali, and F. Alvi. Shock-boundary layer interaction due to a sharp unswept fin in a Mach 2 flow. In *53rd AIAA Aerospace Sciences Meeting*, page 1517, 2015.

[26]F. Alvi and G. Settles. Physical model of the swept shock wave/boundary-layer interaction flowfield. *AIAA journal*, 30(9):2252–2258, 1992.

[27]N. Arora, M. Ali, and F. Alvi. Flowfield of a 3-D swept shock boundary layer interaction in a Mach 2 flow. In *46th AIAA Fluid Dynamics Conference*, page 3649, 2016.

[28]T. Leger, N. Bisek, and J. Poggie. Computations of turbulent flow over a sharp fin at Mach 5. *Journal of Thermophysics and Heat Transfer*, 30(2):394–402, 2016.

[29]E. Schülein. Skin friction and heat flux measurements in shock/boundary layer interaction flows. *AIAA Journal*, 44(8):1732–1741, 2006.

[30]G. Settles. Swept shock/boundary-layer interactions: Scaling laws, flowfield structure, and experimental methods. In *In AGARD, Special Course on Shock-Wave/Boundary-Layer Interactions in Supersonic and Hypersonic Flows 40 p (SEE N94-15196 03-34)*, 1993.

[31]G. Candler, D. Mavriplis, and L. Trevino. Current status and future prospects for the numerical simulation of hypersonic flows. In *47th AIAA Aerospace Sciences Meeting including The New Horizons Forum and Aerospace Exposition*, page 153, 2009.

[32]T. Economon, F. Palacios, S. Copeland, T. Lukaczyk, and J. Alonso. SU2: An open-source suite for multiphysics simulation and design. *AIAA Journal*, 54(3):828–846, 2016.

[33]P. Spalart and S. Allmaras. A one-equation turbulence model for aerodynamic flows. In *30th aerospace sciences meeting and exhibit*, page 439, 1992.

[34]P. Roe. Approximate riemann solvers, parameter vectors, and difference schemes. *Journal of computational Physics*, 43(2):357–372, 1981.

[35]M-S. Liou and C. Steffen Jr. A new flux splitting scheme. *Journal of computational Physics*, 1991.

[36]M-S. Liou. A sequel to AUSM: AUSM+. *Journal of computational Physics*, 129(2):364–382, 1996.

[37]M-S. Liou. A sequel to AUSM, part II: AUSM+ up for all speeds. *Journal of Computational Physics*, 214(1):137–170, 2006.

[38]V. Venkatakrishnan. On the accuracy of limiters and convergence to steady state solutions. In *31st Aerospace Sciences Meeting*, page 880, 1993.

[39]A. Trettel and J. Larsson. Mean velocity scaling for compressible wall turbulence with heat transfer. *Physics of Fluids*, 28(2):026102, 2016.

[40]H. Yan, D. Gaitonde, and J. Shang. Investigation of localized arc filament plasma actuator in supersonic boundary layer. In *45th AIAA Aerospace Sciences Meeting and Exhibit*, page 1234, 2007.

[41]H. Yan and D. Gaitonde. Effect of thermally induced perturbation in supersonic boundary layers. *Physics of Fluids*, 22(6):064101, 2010.

[42]H. Yan and D. Gaitonde. Parametric study of pulsed thermal bumps in supersonic boundary layer. *Shock Waves*, 21(5):411–423, 2011.

[43]B. Edney. Anomalous heat transfer and pressure distributions on blunt bodies at hypersonic speeds in the presence of an impinging shock. Technical report, Flygtekniska Forsoksanstalten, Stockholm (Sweden), 1968.

[44]S. Garg and G. Settles. Unsteady pressure loads generated by swept-shock-wave/boundary-layer interactions. *AIAA Journal*, 34(6):1174–1181, 1996.